optica

Electrically injected GeSn lasers on Si operating up to 100 K

Yiyin Zhou,[1,2] Yuanhao Miao,[1] Solomon Ojo,[1,2] Huong Tran,[1] Grey Abernathy,[1,2] Joshua M. Grant,[1,2] Sylvester Amoah,[1] Gregory Salamo,[3,4] Wei Du,[5] Jifeng Liu,[6] Joe Margetis,[7] John Tolle,[7] Yong-hang Zhang,[7] Greg Sun,[8] Richard A. Soref,[8] Baohua Li,[9] and Shui-Qing Yu[1,4,*]

[1]Department of Electrical Engineering, University of Arkansas, Fayetteville, Arkansas 72701, USA
[2]Microelectronics-Photonics Program, University of Arkansas, Fayetteville, Arkansas 72701, USA
[3]Department of Physics, University of Arkansas, Fayetteville, Arkansas 72701, USA
[4]Institute for Nanoscience and Engineering, University of Arkansas, Fayetteville, Arkansas 72701, USA
[5]Department of Electrical Engineering and Physics, Wilkes University, Wilkes-Barre, Pennsylvania 18766, USA
[6]Thayer School of Engineering, Dartmouth College, Hanover, New Hampshire 03755, USA
[7]School of Electrical, Energy and Computer Engineering, Arizona State University, Tempe, Arizona 85287, USA
[8]Department of Engineering, University of Massachusetts Boston, Boston, Massachusetts 02125, USA
[9]Arktonics, LLC, 1339 South Pinnacle Drive, Fayetteville, Arkansas 72701, USA
*Corresponding author: syu@uark.edu

Received 20 April 2020; revised 1 July 2020; accepted 1 July 2020 (Doc. ID 395687); published 5 August 2020

Monolithic lasers on Si have long been anticipated as an enabler of full photonic integration, and significant progress in GeSn material development shows promise for such laser devices. While there are many reports focused on optically pumped lasers, in this work, we demonstrate electrically injected GeSn lasers on Si. We grew a GeSn/SiGeSn heterostructure diode on a Si substrate in a ridge waveguide laser device and tested it under pulsed conditions, giving consideration to the structure design to enhance the carrier and optical confinement. The peak linewidth of 0.13 nm (0.06 meV) and injection current curves indicated lasing, which was observed up to 100 K with emission peaks at 2300 nm. We recorded a threshold of 598 A/cm^2 at 10 K. The peak power and external quantum efficiency were 2.7 mW/facet and 0.3%, respectively. The results indicate advances for group-IV-based lasers, which could serve as a promising route for laser integration on Si.

https://doi.org/10.1364/OPTICA.395687

1. INTRODUCTION

Research advance in GeSn semiconductors has opened a new avenue for the development of Si-based optoelectronic devices [1–3]. With Sn content over 8%, GeSn turns into a direct bandgap material, which is essential for efficient light emission. Furthermore, the GeSn epitaxy is monolithic on Si and fully compatible with complementary metal-oxide semiconductors. The broad wavelength coverage also makes it versatile for mid-infrared applications, such as bio/chemical sensing, spectroscopy, and pyrometry [4,5]. All these advantages make GeSn material a promising candidate for the integrated light source on the Si platform that enables the system to be more compact, low cost, efficient, and reliable.

In the last few years, there was considerable progress in the development of optically pumped GeSn lasers. The first GeSn laser was presented with a 12.6% Sn composition operating at temperatures up to 90 K [6]. Later, higher Sn incorporation was reported to be beneficial on elevating the lasing temperature [7,8]. Further attempts on 20% Sn incorporation resulted in near-room-temperature lasing operation [9]. SiGeSn/GeSn heterostructure and multiple-quantum-well lasers were achieved with reduced threshold [10,11] as well as elevated operating temperatures [12]. Efforts on strain engineering of the GeSn lasers showed great improvements in device performance as an alternative route to incorporating more Sn. Chrétien *et al.* showed the laser operating temperature as high as 273 K with 16% Sn composition [13]. A continuous-wave optically pumped laser was reported with Sn composition as low as 5.4% in a tensile strained disk structure [14]. Thus far, all GeSn lasers were reported using optical pumping and how to achieve electrically injected lasers as predicted earlier [15,16] remains elusive.

Here we present the first demonstration of electrically injected GeSn diode lasers. The GeSn/SiGeSn double heterostructure was grown, which ensures the carrier-and-optical confinement. To address the hole leakage due to a type II band alignment between GeSn and the top SiGeSn barrier, the p-type top SiGeSn layer was designed to facilitate the hole injection. The ridge waveguide

GeSn lasers were fabricated, and pulsed lasing was observed up to 100 K. The threshold was measured at 598 A/cm^2 at 10 K. The characteristic temperature T_0 was extracted from 76 to 99 K at the temperature range of 10 to 77 K for different devices.

2. EXPERIMENT

The laser diode structure was grown via an industry-standard chemical vapor deposition reactor using commercially available precursors on a 200 mm (100) Si substrate. Five epitaxial layers were grown from bottom to top: i) a nominal 500 nm thick strain-relaxed Ge buffer layer, with n-type doping of 1×10^{19} cm^{-3}; ii) a 700 nm thick GeSn buffer layer using the spontaneous relaxation enhanced growth method [17], with nominal Sn composition from 8% (bottom) to 11% (top) and n-type doping of 1×10^{19} cm^{-3}; iii) a nominally intrinsic 1000 nm thick $Ge_{0.89}Sn_{0.11}$ active layer; iv) a 170 nm $Si_{0.03}Ge_{0.89}Sn_{0.08}$ cap layer with p-type doping of 1×10^{18} cm^{-3}; and v) a 70 nm $Si_{0.03}Ge_{0.89}Sn_{0.08}$ ohmic contact layer with p-type doping of 1×10^{19} cm^{-3}. All doping growth was done *in situ* by introducing corresponding doping gases. The cross-sectional schematic of the laser device is shown in Fig. 1(a). The compositions of Sn and the layer thickness were measured by x-ray diffraction and transmission electron microscopy techniques (see Supplement 1 Sections 1 and 2 for details).

After the growth, the sample was fabricated into ridge waveguide laser structures and then cleaved into individual devices with the cavity lengths of 0.3, 0.5, 0.8, and 1.7 mm. The 80 μm wide ridges were formed by wet etching. The etching depth was controlled at 1.4 μm to expose the GeSn buffer layer for metal contacts. Electron beam evaporated Cr and Au were deposited as both p and n electrodes through a liftoff process with the thickness of 10 nm and 350 nm, respectively. The Si substrate was lapped down to 140 μm thick, followed by cleaving to form the Fabry–Perot cavity. Finally, the devices were wire-bonded to a Si chip carrier and mounted in a cryostat for low-temperature measurements.

The current-voltage (IV) measurement was performed using a direct current source measurement unit. For the pulsed measurement, a pulsed high-compliance voltage source was used to drive the laser, and the current was monitored by a calibrated magnetically coupled current meter. The repetition rate of 1 kHz and pulse width of 700 ns were used for the spectra and light output versus injection current (LI) measurements. The electroluminescence and photoluminescence (PL) emission signal was collected and analyzed through a monochromator (10 nm resolution) and liquid-nitrogen-cooled InSb detector (response range 1–5.5 μm). The high-resolution spectra were obtained by using a Fourier-transform infrared spectroscopy (FTIR) instrument equipped with the InSb detector. Step-scan mode was used with a 0.25 cm^{-1} resolution for the measurement.

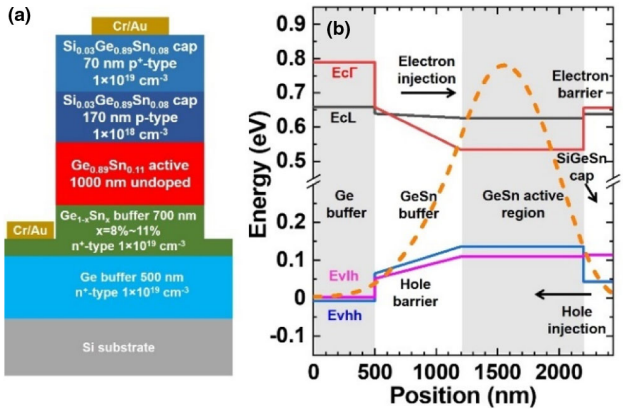

Fig. 1. (a) Cross-sectional schematic of laser device; (b) Calculations of band structure and profile of fundamental TE mode. Band structure shows type II alignment between GeSn active and SiGeSn cap layers at LH band. Mode profile shows 75% of the optical field overlapped with the GeSn active region.

3. RESULTS

The device band edge diagram at 300 K was calculated based on the method described in Ref. [18] and plotted in Fig. 1(b). Four subbands including indirect L (E_{cL}) and direct Γ ($E_{c\Gamma}$) valleys in the conduction band (CB) and heavy hole (E_{vhh}) and light hole (E_{vlh}) in the valence band (VB) were considered. The following features are obtained from Fig. 1(b): i) the $Ge_{0.89}Sn_{0.11}$ active layer has a direct bandgap with the energy difference of 92 meV between the L and Γ valleys. The high degree of relaxation in this layer results in the small difference between heavy hole (HH) and light hole (LH) band. ii) In the CB, both the Γ and L valleys feature type I alignment due to the wider bandgap energies of the $Si_{0.03}Ge_{0.89}Sn_{0.08}$ cap and the GeSn buffer. Note that the Sn composition increases in the GeSn buffer (8%∼11%) along the growth direction, leading to the decrease of both Γ and L valleys in energy with Γ more rapidly than the L valley. iii) In the VB, the HH band features type I band alignment. The LH exhibits type II band alignment at the cap/active layer interface due to the tensile strain within the $Si_{0.03}Ge_{0.89}Sn_{0.08}$ cap.

The fundamental TE mode was plotted (dashed curve) to show the optical field distribution. The refractive index for each layer was taken from our previous study [19]. The optical confinement factor (optical field confined in the $Ge_{0.89}Sn_{0.11}$ active region) was calculated as 75% using the wavelength at 2.3 μm.

The typical pulsed LI curves from the 0.8 mm cavity length device were plotted in Fig. 2(a) at temperatures from 10 to 100 K (maximum lasing temperature). The threshold current densities are measured as 0.74 and 3.9 kA/cm^2 at 10 and 100 K, respectively.

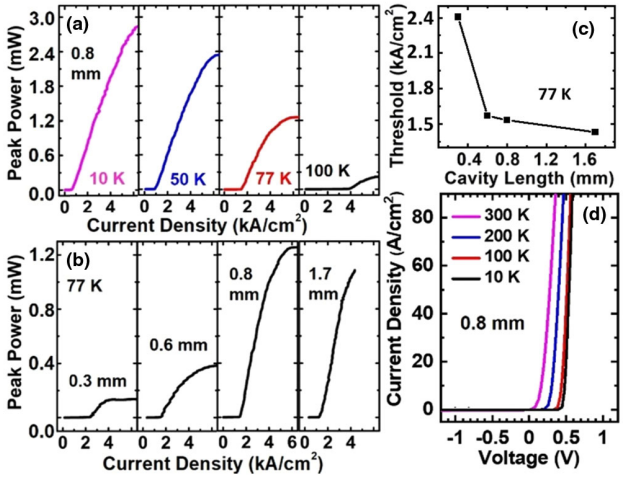

Fig. 2. (a) LI curves of the 0.8-mm cavity length device from 10 to 100 K; (b) LI curves at 77 K for four devices with different cavity lengths; (c) Threshold of each device at 77 K; (d) Temperature-dependent IV of the 0.8-mm cavity length device.

At 10 K, the emission shows a saturation feature at 7.5 kA/cm^2. The maximum peak power was measured as 2.7 mW/facet.

The LI characteristics of devices with different cavity lengths were studied, as shown in Fig. 2(b), at 77 K. The threshold current densities were measured as 2.4, 1.6, 1.5, and 1.4 kA/cm^2 for devices with cavity lengths of 0.3, 0.6, 0.8, and 1.7 mm, respectively, as shown in Fig. 2(c). As cavity length (L) increases, the decreased lasing threshold is mainly due to the reduced mirror loss ($\propto 1/L$). The 1.7 mm device has the lowest threshold among four devices, with the value of 598 A/cm^2 at 10 K. The temperature-dependent thresholds for all four devices were extracted and summarized (see Supplement 1 Section 6 for details). Moreover, the saturated emission intensity increases as L increases, except for the 1.7 mm device (no higher current could be applied due to device damage).

The typical IV characteristics of the 0.8 mm cavity length device were measured at various temperatures as plotted in Fig. 2(d). The series resistance is extracted as 1.2 Ω at 10 K. The IV characteristics are consistent with our previous GeSn diode studies [20,21], where the detailed IV analysis was reported. Under the pulsed current operation, low duty cycle and short pulse width were chosen to minimize the joule heating.

The emission spectra below and above threshold were investigated. Figure 3(a) shows the spectra of the 0.3 mm cavity length device under various current injection levels at 10 K. Below the threshold, the peak full width at half-maximum (FWHM) was 64 nm, while above the threshold the FWHM became ~20 nm as shown in Fig. 3(a) inset. Note that the relative broad peak linewidth of 20 nm is due to the spectral resolution of 10 nm. At 10 K, the lasing emission peak was observed at 2250 nm.

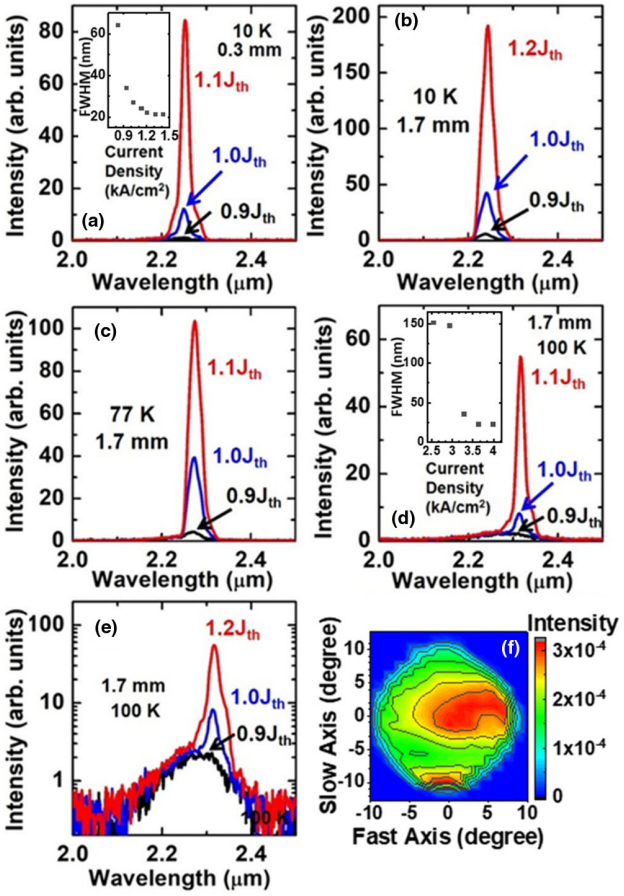

Fig. 3. Emission spectra at various current injection levels. (a) 0.3-mm device at 10 K. Inset: extracted FWHM versus current density (spectral resolution of 10 nm); (b), (c), and (d) 1.7-mm device at 10 K, 77 K, and 100 K. Inset in (d): extracted FWHM vs current density; (e) log-scale plot of spectra in (d); (f) far field pattern from 1.7-mm device at 77 K.

Figures 3(b)–3(d) show the emission spectra of the 1.7 mm cavity length device at 10, 77, and 100 K, respectively. At each temperature, as the injection current density increases from below to above the threshold, the significantly increased peak intensity and reduced FWHM were observed, both being evidence of the lasing characteristic. At 10 K, the measured peak position is the same as for the 0.3 mm device, i.e., at 2250 nm. At 100 K, the lasing peak redshifts to 2300 nm as expected due to the narrowed bandgap. The log-scale plot of Fig. 3(d) is shown in (e). Above the threshold, the stimulated emission peak stands out from the broad spontaneous emission.

The far-field pattern was measured at the cross-section plane 4 cm away from the laser facet. Two major peaks were observed, indicating multimode operation as shown in Fig. 3(f). The FWHMs of the major peak at the center are estimated around 16 and 12 deg along the fast and slow axis, respectively.

To further study the lasing characteristic, high-resolution spectra were measured using a FTIR. Figure 4 shows the spectra of the 0.8 mm cavity length device at 77 K under various current injections. Above the threshold, the multimode lasing characteristic was clearly observed. The minimum FWHM of the individual peak is measured as 0.13 nm (or 0.06 meV). The dramatically reduced peak linewidth under higher injection is one of the lasing characteristics. At above 1.42 × threshold, the peak at 2307 nm dominates the lasing spectrum.

The temperature-dependent threshold for each device was analyzed. The characteristic temperature T_0 was extracted using the empirical relation [22] $J_{th} = J_0 exp(T/T_0)$, where J_{th} is the threshold current density, J_0 is a constant, and T is the temperature. For each device, two regions, from 10 K to 77 K and from 77 K to 100 K can be clearly observed as shown in Fig. 5 (except the 0.3 mm device, whose maximum lasing temperature is 90 K). From 10 K to 77 K, three devices (0.3, 0.6, and 0.8 mm) exhibited T_0 above 90 K, while the 1.7 mm device showed T_0 of 76 K. From 77 K to 100 K, three devices show T_0 values close to ~30 K as a result of the significantly increased threshold.

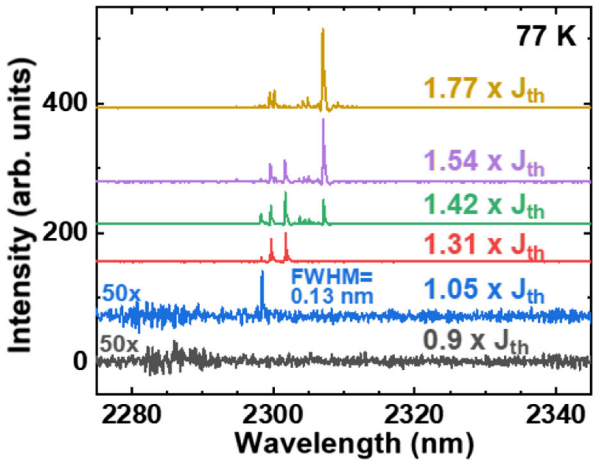

Fig. 4. High-resolution spectra of 0.8-mm cavity length device at 77 K under various current injections.

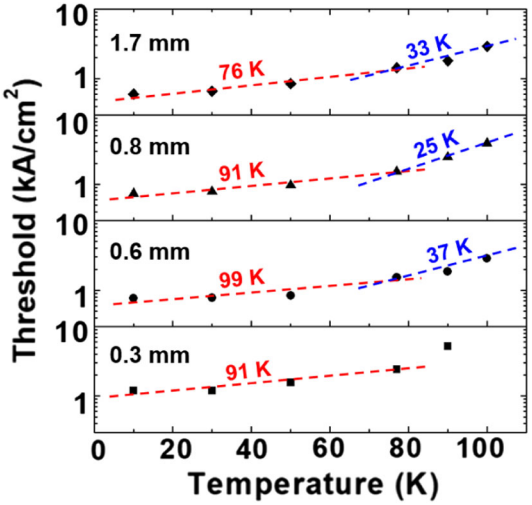

Fig. 5. Extracted T_0 for each device. For the 0.3-mm device, the data point of threshold at 90 K was excluded from data fitting.

4. DISCUSSION

In comparison with obtaining optically pumped lasers, there are special considerations for both carrier confinement and optical confinement in this work for the device structure design. In considering the carrier confinement in these laser devices, the result of the band structure calculation shown in Fig. 1(b) reveals that a type II band alignment between the GeSn active and SiGeSn cap layers in LH at VB. The type II alignment is originated from the tensile strain of the SiGeSn cap lifting the LH band above that in the GeSn active layer. As a result, the hole leakage at the top surface could lead to an increase in the lasing threshold. Therefore, this design is not ideal for optically pumped devices. However, for electrically injected devices, in order to address this poor hole-confinement issue, the top SiGeSn layer was intentionally doped as *p* type in this work. As the holes are injected from the top SiGeSn cap layer, they are forced to flow to the GeSn active region. Since there are hole barriers in both HH and LH bands at VB between GeSn active and GeSn buffer layers, the holes could be confined in the active region to facilitate the population inversion. While the electrons are injected from the bottom GeSn buffer with the n-type contact, the electron barrier in Γ valley (lower band than L valley) in CB between the GeSn active and the top SiGeSn cap prevent the leakage of electrons and confine them in the active region. This p-i-n device structure design, rather than the n-i-p structure, which may utilize the p-type unintentional background doping of the GeSn buffer, effectively minimizes the hole leakage and enhances the carrier confinement. Similar asymmetric confinement structure design can be found in early III-V double-heterostructure lasers [23,24].

In order to increase the optical confinement, it is necessary to address the small difference in the refractive index between Ge (4.03 at 2.3 μm) and GeSn (4.1∼4.2 with different Sn %). To increase the mode overlap with the GeSn active layer, an overall 240 nm thick SiGeSn cap layer was grown on top of the GeSn active layer, which pushes the peak intensity of the optical field into the active region, resulting in a 75% mode overlap with the GeSn core layer whose thickness is 1000 nm as shown in Fig. 1(a). For optically pumped laser devices, the optical field can be well confined since there is nothing but the air above the cap layer. However, for the electrically injected laser devices, due to the metal contact above the cap layer, the thickness of the SiGeSn cap needs to be carefully optimized to minimize the optical loss via the metal thin film. The current thickness is selected as a compromise of the SiGeSn growth capability and the metal optical loss.

The lasing spectra were further examined with the PL study of the active region (see Supplement 1 Section 4 for details). The lasing peak from the 0.8 mm cavity length device features a narrow linewidth (∼23 nm) compared to that of the PL spectrum (205 nm). In addition, the 77 K high-resolution spectra in Fig. 4 reveals the details of the spectrum, where the multiple longitudinal peaks (with subnanometer individual peaks) form an envelope that shown as a single peak in the low-resolution measurement. The dramatic reduction of peak linewidth indicates the onset of lasing.

T_0 of ∼90 K in the temperature range below 77 K is comparable with earlier reported III-V double heterostructure laser diodes [23,25]. As temperature increases above 77 K, the carriers in the GeSn active region could gain sufficient thermal energy to overcome the barriers and leak into the SiGeSn cap and GeSn buffer layers, resulting in significantly increased lasing threshold. This leads to the considerably reduction of T_0 above 77 K, ranging from 25 K to 37 K as shown in Fig. 5. By optimizing the design of the cap and buffer layers, the improved carrier confinement at higher temperatures can be obtained, and thus higher T_0 is expected.

Note that although 2.7 mW/facet peak power was obtained, the external quantum efficiency (EQE) was estimated as 0.3% (both facets power counted), which is relatively low even compared with early reported III-V double-heterostructure lasers [23]. This might be attributed to low injection efficiency due to the material band structure (close to indirect bandgap), current leakage due to poor carrier confinement, and the high internal optical loss. A thorough study will be the next step to quantitatively investigate the origin of low EQE.

To further improving the device performance, investigations of new structure designs are underway, which include: i) increasing the Sn content to increase the bandgap directness so that injection efficiency can be increased; ii) adding an SiGeSn buffer on the *n* layer to enhance the hole confinement; iii) improving material quality and fabrication technique to minimize the interface defects and surface roughness so that internal optical loss can be reduced; and iv) reducing doping levels to minimize the free carrier absorption.

5. CONCLUSION

We have demonstrated electrically injected GeSn/SiGeSn heterostructure lasers that were grown on a Si wafer using a commercial CVD reactor. The narrow peak linewidth of 0.13 nm (0.06 eV) and LI curve characteristics evidentially confirm the lasing. The multimode lasing characteristics were observed by high-resolution spectra. The lasing threshold of 598 A/cm^2 at 10 K was obtained. The maximum lasing temperature was measured as 100 K with 2300 nm peak wavelength. The p−i−n structure design enhances the carrier confinement by reducing the hole leakage through the type II band aligned cap layer. The peak power was measured as 2.7 mW/facet at 10 K, corresponding to calculated EQE of ∼0.3%.

Funding. Air Force Office of Scientific Research (FA9550-18-1-0045, FA9550-19-1-0341).

Acknowledgment. Dr. Wei Du appreciates support from Provost's Research & Scholarship Fund at Wilkes University.

Disclosures. The authors declare no conflicts of interest.

See Supplement 1 for supporting content.

REFERENCES

1. S. Wirths, D. Buca, and S. Mantl, "Si–Ge–Sn alloys: from growth to applications," Prog. Cryst. Growth Charact. Mater. **62**, 1–39 (2016).
2. R. Soref, D. Buca, and S. Yu, "Group IV photonics: driving integrated optoelectronics," Opt. Photon. News **27**(1), 32–39 (2016).
3. J. Zheng, Z. Liu, C. Xue, C. Li, Y. Zuo, B. Cheng, and Q. Wang, "Recent progress in GeSn growth and GeSn-based photonic devices," J. Semicond. **39**, 061006 (2018).
4. R. Soref, "Mid-infrared photonics in silicon and germanium," Nat. Photonics **4**, 495–497 (2010).
5. X. Wang and J. Liu, "Emerging technologies in Si active photonics," J. Semicond. **39**, 061001 (2018).
6. S. Wirths, R. Geiger, N. von den Driesch, G. Mussler, T. Stoica, S. Mantl, Z. Ikonic, M. Luysberg, S. Chiussi, J. M. Hartmann, H. Sigg, J. Faist, D. Buca, and D. Grützmacher, "Lasing in direct-bandgap GeSn alloy grown on Si," Nat. Photonics **9**, 88–92 (2015).
7. V. Reboud, A. Gassenq, N. Pauc, J. Aubin, L. Milord, Q. M. Thai, M. Bertrand, K. Guilloy, D. Rouchon, J. Rothman, T. Zabel, F. Armand Pilon, H. Sigg, A. Chelnokov, J. Hartmann, and V. Calvo, "Optically pumped GeSn micro-disks with 16% Sn lasing at 3.1 μm up to 180 K," Appl. Phys. Lett. **111**, 092101 (2017).
8. J. Margetis, S. Al-Kabi, W. Du, W. Dou, Y. Zhou, T. Pham, P. Grant, S. Ghetmiri, A. Mosleh, B. Li, J. Liu, G. Sun, R. Soref, J. Tolle, M. Mortazavi, and S. Yu, "Si-based GeSn lasers with wavelength coverage of 2–3 μm and operating temperatures up to 180 K," ACS Photon. **5**, 827–833 (2017).
9. Y. Zhou, W. Dou, W. Du, S. Ojo, H. Tran, S. Ghetmiri, J. Liu, G. Sun, R. Soref, J. Margetis, J. Tolle, B. Li, Z. Chen, M. Mortazavi, and S. Yu, "Optically pumped GeSn lasers operating at 270 K with broad waveguide structures on Si," ACS Photon. **6**, 1434–1441 (2019).
10. D. Stange, N. von den Driesch, T. Zabel, F. Armand-Pilon, D. Rainko, B. Marzban, P. Zaumseil, J. Hartmann, Z. Ikonic, G. Capellini, S. Mantl, H. Sigg, J. Witzens, D. Grützmacher, and D. Buca, "GeSn/SiGeSn heterostructure and multi quantum well lasers," ACS Photon. **5**, 4628–4636 (2018).
11. J. Margetis, Y. Zhou, W. Dou, P. Grant, B. Alharthi, W. Du, A. Wadsworth, Q. Guo, H. Tran, S. Ojo, G. Abernathy, A. Mosleh, S. Ghetmiri, G. Thompson, J. Liu, G. Sun, R. Soref, J. Tolle, B. Li, M. Mortazavi, and S. Yu, "All group-IV SiGeSn/GeSn/SiGeSn QW laser on Si operating up to 90 K," Appl. Phys. Lett. **113**, 221104 (2018).
12. Q. Thai, N. Pauc, J. Aubin, M. Bertrand, J. Chrétien, V. Delaye, A. Chelnokov, J. Hartmann, V. Reboud, and V. Calvo, "GeSn heterostructure micro-disk laser operating at 230 K," Opt. Express **26**, 32500–32508 (2018).
13. J. Chrétien, N. Pauc, F. Armand Pilon, M. Bertrand, Q. Thai, L. Casiez, N. Bernier, H. Dansas, P. Gergaud, E. Delamadeleine, R. Khazaka, H. Sigg, J. Faist, A. Chelnokov, V. Reboud, J. Hartmann, and V. Calvo, "GeSn lasers covering a wide wavelength range thanks to uniaxial tensile strain," ACS Photon. **6**, 2462–2469 (2019).
14. A. Elbaz, D. Buca, N. von den Driesch, K. Pantzas, G. Patriarche, N. Zerounian, E. Herth, X. Checoury, S. Sauvage, I. Sagnes, A. Foti, R. Ossikovski, J. Hartmann, F. Boeuf, Z. Ikonic, P. Boucaud, D. Grützmacher, and M. El Kurdi, "Ultra-low threshold cw and pulsed lasing in tensile strained GeSn alloys," Nat. Photonics **14**, 375–382 (2020).
15. G. Sun, R. A. Soref, and H. H. Cheng, "Design of an electrically pumped SiGeSn/GeSn/SiGeSn double-heterostructure mid-infrared laser," J. Appl. Phys. **108**, 033107 (2010).
16. G. Sun, R. A. Soref, and H. H. Cheng, "Design of a Si-based lattice-matched room-temperature GeSn/GeSiSn multi-quantum-well mid-infrared laser diode," Opt. Express **18**, 19957–19965 (2010).
17. W. Dou, M. Benamara, A. Mosleh, J. Margetis, P. Grant, Y. Zhou, S. Al-Kabi, W. Du, J. Tolle, B. Li, M. Mortazavi, and S. Yu, "Investigation of GeSn strain relaxation and spontaneous composition gradient for low-defect and high-Sn alloy growth," Sci. Rep. **8**, 5640 (2018).
18. G. Sun, H. H. Cheng, J. Menéndez, J. B. Khurgin, and R. A. Soref, "Strain-free Ge/GeSiSn quantum cascade lasers based on L-valley intersubband transitions," Appl. Phys. Lett. **90**, 251105 (2007).
19. H. Tran, W. Du, S. Ghetmiri, A. Mosleh, G. Sun, R. Soref, J. Margetis, J. Tolle, B. Li, H. Naseem, and S. Yu, "Systematic study of $Ge_{1-x}Sn_x$ absorption coefficient and refractive index for the device applications of Si-based optoelectronics," J. Appl. Phys. **119**, 103106 (2016).
20. Y. Zhou, W. Dou, W. Du, T. Pham, S. Ghetmiri, S. Al-Kabi, A. Mosleh, M. Alher, J. Margetis, J. Tolle, G. Sun, R. Soref, B. Li, M. Mortazavi, H. Naseem, and S. Yu, "Systematic study of GeSn heterostructure-based light-emitting diodes towards mid-infrared applications," J. Appl. Phys. **120**, 023102 (2016).
21. H. Tran, T. Pham, J. Margetis, Y. Zhou, W. Dou, P. Grant, J. Grant, S. Al-Kabi, G. Sun, R. Soref, J. Tolle, Y. Zhang, W. Du, B. Li, M. Mortazavi, and S. Yu, "Si-Based GeSn photodetectors toward Mid-infrared imaging applications," ACS Photon. **6**, 2807–2815 (2019).
22. J. Pankove, "Temperature dependence of emission efficiency and lasing threshold in laser diodes," IEEE J. Quantum Electron. **4**, 119–122 (1968).
23. I. Hayashi and M. B. Panish, "GaAs–$Ga_xAl_{1-x}As$ heterostructure injection lasers which exhibit low thresholds at room temperature," J. Appl. Phys. **41**, 150 (1970).
24. I. Hayashi, M. B. Panish, and F. K. Reinhart, "GaAs–$Al_xGa_{1-x}As$ double heterostructure injection lasers," J. Appl. Phys. **42**, 1929 (1971).
25. C. J. Nuese, M. Ettenberg, and G. Olsen, "Room-temperature heterojunction laser diodes from vapor-grown $In_{1-x}Ga_xP$/GaAs structures," Appl. Phys. Lett. **25**, 612 (1974).